Investigation of multiferroic properties of dysprosium substituted bismuth ferrite (Bi$_{1-x}$Dy$_x$FeO$_3$) prepared by auto combustion technique

S. Iqbal [a*], H. M. Rafique [a] , G. Hussain [b], I. Ahmed [b], A. Fareed [c]
[a]*Department of Physics, University of the Punjab, Quaid-e-Azam Campus Lahore-54590, Pakistan*
[b]*Department of Physics, University of Agriculture Faisalabad-38040 Pakistan*
[c]*Department of Physics, Government College University Faisalabad-38000, Pakistan*

A simple and inexpensive auto combustion procedure was used to create the Bi$_{1-x}$Dy$_x$FeO$_3$ (x=0.0, 0.015, 0.03, 0.045, 0.060) multiferroics samples. In bismuth ferrite, the average crystallite size increased with growing Dy^{3+} concentration in BFO, revealing a rhombohedral distorted perovskite structure of space group R3c. During morphological analyses of the produced samples, a spherical structure with little aggregation was found. When Dy^{3+} is substituted at the B-site, the Raman modes widen and the cation site occupancy changes even more. The frequency-dependent dielectric properties (ε_r, tanδ), electric conductivity (ac), impedance (Z), and electric modulus (M' and M″) of the samples were assessed using an impedance analyzer at frequencies between 20 Hz and 20 MHz. All samples had the maximum dielectric constant, which was discovered at a relatively low frequency. The highest value of impedance was found at low frequency and it lowers with increasing frequency as a result of the contributions from the grain and grain boundary. It is discovered that the samples' ac conductivity is frequency-dependent and changes depending on how much Dy^{3+} is doped into the BFO.

1. Introduction

Materials with two ferroic characteristics in a single phase are referred to as multiferroic materials. Ferroelectricity, ferroelectricity, ferro periodicity, and ferro elasticity are a few examples of ferroic qualities. Magneto-electric (ME) multiferroics are substances that possess both ferroelectricity and ferromagnetism. The ME effect initiates a single-phase interaction between magnetic and electrical forces. This ME effect, which forms the basis of ME MFs, adds another level of freedom by enabling magnetic spins to be influenced by an electric and magnetic field, respectively. Due to the significant macroscopic behavior of ferroelectricity and magnetism in these compounds, as described by Hill [1,2], ME multiferroics are rare in nature [3]. ME materials are used in a variety of applications and have a broad range of properties. Examples of typical consumer products include quantum electromagnets, storage devices, magnetic field sensors, television, optical fibers, switches, microwave actuators, satellite communication, multiple state memory, spintronic, microelectronic, and high-density ferroelectric RAM devices [4-6]. Among active MFs, bismuth ferrite (BFO) is the storage medium that simultaneously reflects ferroelectric and G-type anti-ferroic properties. A space group and a rhombohedral distorted perovskite structure are present in the chamber of the temperature BFO 3. To tackle the problem of synthesizing BFO in the pure phase, researchers explored a range of preparation procedures, including coprecipitation [7], solid-state reaction [8], hydrothermal [9], sol-gel auto combustion method [10], and micro-emulsion [11]. Because it has so many benefits over other preparation methods, such as low cost, ease of use, consistency, and so on, the auto combustion process is

being employed extensively [12]. Dhir and others, [24] Sol-gel analysis was used to describe the peak shifts caused by the substitution of Dy^{3+} ions in $Bi_{1-x}Dy_xFeO_3$ (x = 0.0, 0.10). The generated nanoparticles' dielectric behavior was confirmed. Li et al. claim that Mg^{2+} doped $BiFeO_3$ has outstanding ferroelectric and magnetic properties, making it a good choice for use in magnetoelectric and data storage devices [13,14]. The Dy^{3+} doped $Bi_{1-x}Dy_xFeO_3$ (x =0.00, 0.015, 0.03, 0.045, and 0.06) has been synthesized in the current study, and its structural, morphological, and dielectric properties have been investigated for its practical applications.

2. Materials and method

2.1. Synthesis of dysprosium substituted BFO

The multiferroics $Bi_{1-x}Dy_xFeO_3$ were produced by sol-gel auto combustion for x=0.0, 0.015, 0.03, 0.045, and 0.06. The first components utilized to make multiferroics were iron nitrate nonahydrate, bismuth nitrate hexahydrate, strontium nitrate, nitric acid, citric acid, and ammonia solution. In distilled water, all of the nitrates dissolve. The bismuth nitrate was dissolved in distilled water using a little quantity of nitric acid. For an hour, the nitrates solution has to be blended and stirred. Citric acid is added as the fuel agent, and the pH is maintained at 7 using an ammonia solution. The mixture was then put on a hot plate set at 90°C, where it was stirred and heated until it became a gel. After the gel had formed, the hot plate's temperature was increased to 300 °C. Ash was gathered after the gel had been burnt. A pestle and mortar were used to grind the ash. Three hours were spent in a furnace sintering this powder at 600 degrees Celsius. Now that the final product has been achieved, it may be characterized.
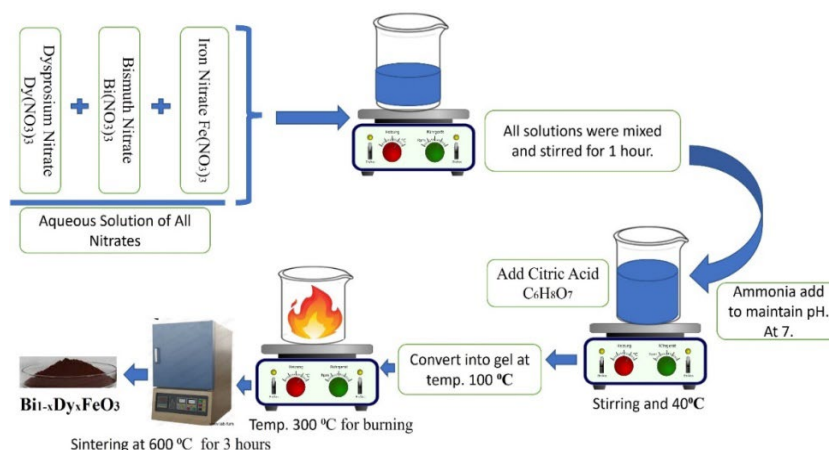

Fig. 1. Synthesis of Dy doped Bismuth ferrites.

The structural characteristics were investigated using an X-ray diffractometer. The JEOL-JSM 5910 model was used to analyze morphological characteristics. The measurements of the dielectric were made using an impedance analyzer. Ferroelectric investigations were conducted using an automated P-E loop tracer.

3. Results and discussion

3.1. Structural analysis

Figure 2 displays an XRD pattern for the $Bi_{1-x}Dy_xFeO_3$ samples produced using the auto combustion method with (x = 0.0, 0.015, 0.03, 0.045, and 0.06). Sharp peaks in XRD patterns are indexed using Miller indices (0 1 2), (1 1 0), (006), (2 0 2), (1 1 6) and (3 0 0). It was discovered that the hexagonal form of $Bi_{1-x}Dy_xFeO_3$ twisted the R3c perovskite structure (BFO). As the

concentration of Dy rises, a few diffraction peaks get weaker and eventually disappear [15]. For samples x = 0.0 to 0.06, no further Dy^{3+} peaks were discovered. However, for the samples, x = 0.0 to x = 0.06 that match to (JCPDS#75-0541), very small intensity peaks were seen between the peaks (012) and (110), and another peak was found between the peaks (110) and (006) with a greater concentration of $Dy^{3+.}$ There are no split peaks; the only apparent peak displacement is in the direction of low theta, or at [1 1 0]. Due to the ionic radius difference between lanthanum (Dy^{3+} = 0.92Å) and iron (Fe^{3+} = 0.67Å), the Dy substitution somewhat changes the intensity of the majority of peaks. The average particle size of BFO is calculated using the Scherrer equation [16].
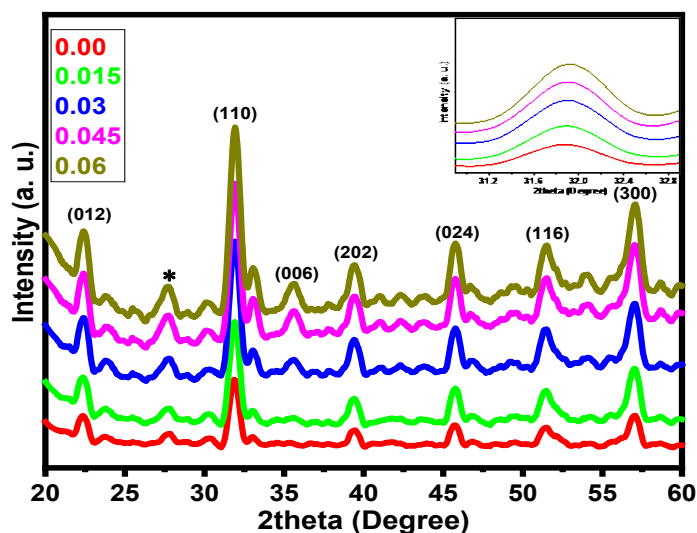

Fig. 2. Shows the XRD pattern of $Bi_{1-x}Dy_xFeO_3$ (x = 0.0, 0.015, 0.03, 0.045, and 0.06) with an inset showing peak shifting at [1 1 0].

3.2. Physical parameters

The average crystallite size of pure and doped BFO is calculated using the Scherrer equation [1][2].

$$D = \frac{k\lambda}{\beta_{hkl}Cos\theta} \tag{1}$$

D, K, and here denote the peak broadening factor, shape factor, average crystallite size, and X-ray wavelength, respectively [16,19,20]. It has been shown that the average crystallite size rises with increasing Dysprosium doping. The relationships are utilized to get the lattice constants (a and c) and cell volume (V) [18].

$$\frac{1}{d^2} = \frac{4}{3}\left[\frac{h^2+hk+k^2}{a^2}\right] + \frac{l^2}{c^2} \tag{2}$$

$$V_{cell} = a^3 \tag{3}$$

The lattice constants (a and c) were discovered to be in the range (a = 5.5638 - 5.5901, c = 13.1878 - 13.6776 (Å)) when the amount of dysprosium substitution in $BiFeO^3$ increases, as shown in table 1. In the range (409.71–412.09 ($Å^3$)), the volume of the unit cell was computed. The X-ray density and bulk density are calculated using the equation shown below [19].

$$d_{x-ray} = \frac{nM}{N_A Vc} \tag{4}$$

$$P_b = \frac{Mass}{Volume} \tag{5}$$

Avogadro's number, the number of atoms in a unit cell, the atomic mass of the sample, and other terms are represented by the letters n, A, V, N_A, m, h, and r. The expected values for the lattice constants, cell volume, X-ray density, bulk density, and porosity are shown in Table.1[18]. The values for the bulk density are 0.7307 and 0.7617 (g/cm^3). Because of the replacement of Rare Earth (Dy^{3+}) ions, which caused such low quantities, grain formation would have been hampered [21-3]. The sample had porosity throughout the synthesis and sintering procedures, which is connected to this.

$$\varepsilon = \frac{1}{d^2} \qquad (6)$$

The value of strain (ε) found in the range of 0.1266 – 0.1296 are shown in Table 1.

Table 1. XRD parameters as of the prepared samples.

Concentrations (x)	D (nm)	a (Å)	c (Å)	Unit cell Volume (Å^3)	X-ray density d_x	Bulk density d_B	Strain (ε)
0.00	7.9079	5.5842	13.1878	412.09	7.56	0.7591	0.1271
0.015	9.6589	5.5638	13.6776	409.71	7.33	0.7617	0.1266
0.03	12.5633	5.5901	13.5269	415.21	7.32	0.7500	0.1287
0.045	37.7272	5.5836	13.1139	423.56	7.21	0.7328	0.1296
0.06	48.9367	5.5765	13.3244	424.26	7.06	0.7307	0.1278

3.3 SEM analysis

SEM is used to analyze the surface morphology of the manufactured Bi$_{1-x}$Dy$_x$FeO$_3$ multiferroics. Due to the magnetic dipole interaction between the ferrite particles, the nanoparticles have a non-homogeneous spherical morphology and some degree of agglomeration. The average grain size of the treated samples is calculated using the line intercept approach, and it is found to be between 0.20 and 0.28 nm as shown in Fig. 3(a,b,c) [20][21].
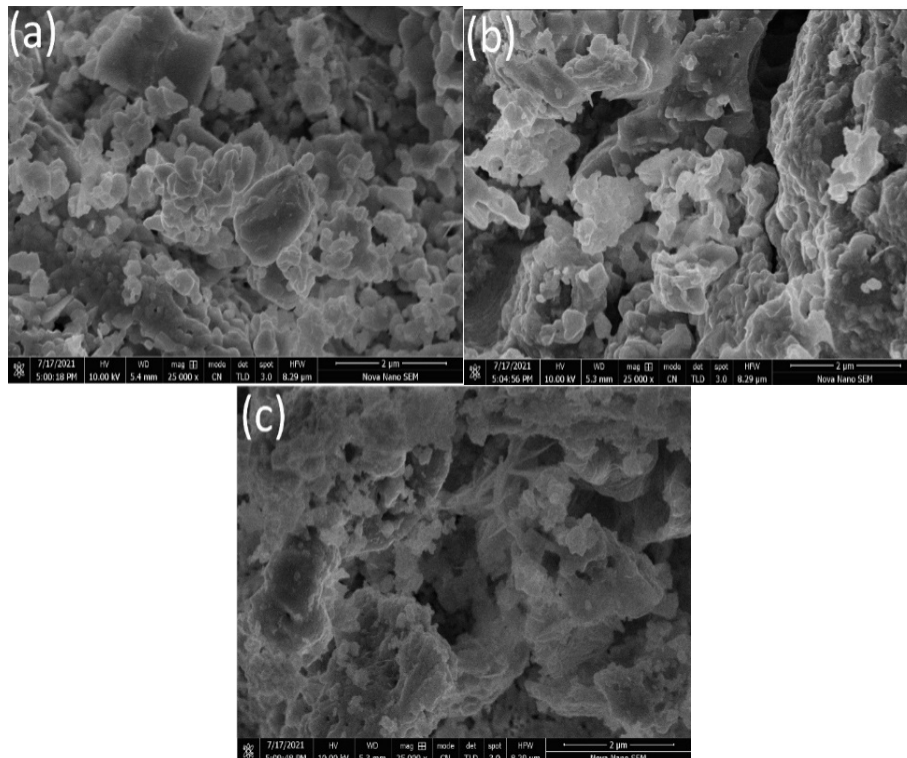

Fig. 2. SEM micrographs of all Bi$_{1-x}$Dy$_x$FeO$_3$ samples (a) x=0.00, (b) x=0.03, (c) = 0.06.

3.4 FTIR analysis

Using the spectroscopic method FTIR, two different vibrational modes that matched the spinel lattice were discovered. Figure 4 displays the 400–4000 cm^{-1} range of the FTIR spectra of Multiferrites powders. The location of metal ions inside the crystal lattice as well as the distribution of cations may be determined using the spectroscopic method known as Fourier transform infrared spectroscopy (FTIR) [22]. v2 denotes the low-frequency absorption band, and v_1 the high-frequency absorption band, as can be observed. Nano ferrite samples have both the higher absorption frequency band of 619.76 - 630.39 cm^{-1} and the lower absorption frequency spectrum of 568.37 to 578.65 cm^{-1}. The octahedral site is related with the lower-frequency absorption bands in the spinel structure of nano ferrites, while the tetrahedral site is associated with the higher-frequency absorption bands [23]. The variety of locations is mostly caused by the variation in bond length and binding strength of these diverse synthetic materials.
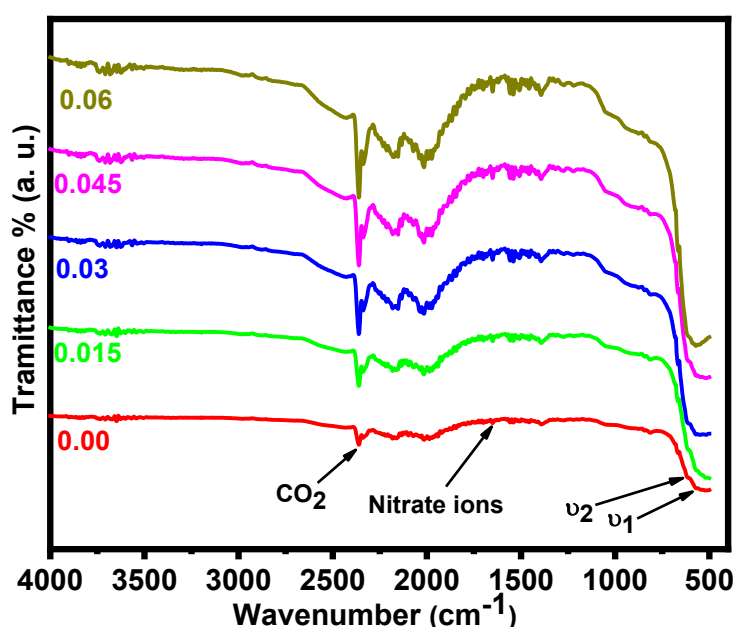

Fig. 4. FTIR spectra of $Bi_{1-x}Dy_xFeO_3$ (x = 0.00, 0.015, 0.03, 0.045 and 0.06).

The differing radii of the dopants Dy^{3+} (0.91 Å) and Fe^{3+} (0.64 Å), which impact Fe^{3+}- O_2, might be the cause of the disparity in wavenumber. The sample had several vibrational bands as well. While the doublet peak at 2361 cm^{-1} is brought on by ambient CO_2 gas, the bands started to develop about 1662 as a result of the stretching vibration of nitrate ions [24, 25].

3.5 UV–visible spectroscopy analysis

The UV-vis pattern of Dy^{3+} doped BFO ferrite samples is shown in Fig. 5. The KubelkaMunk function is used to compute the absorption coefficient (α):

$$\alpha = \frac{1-R^2}{R} \tag{7}$$

where R stands for the quantity of reflected light that was measured. The formula for calculating bandgap values for all of the processed samples is as follows:

$$\alpha h\upsilon = B(h\upsilon - Eg)^n \tag{8}$$

where, respectively, the absorption coefficient, incoming photon energy, absorption edge width parameter, energy bandgap, and exponent based on direct and indirect transition across the energy bandgap are represented by the letters, h, B, Eg, and n [26][27].
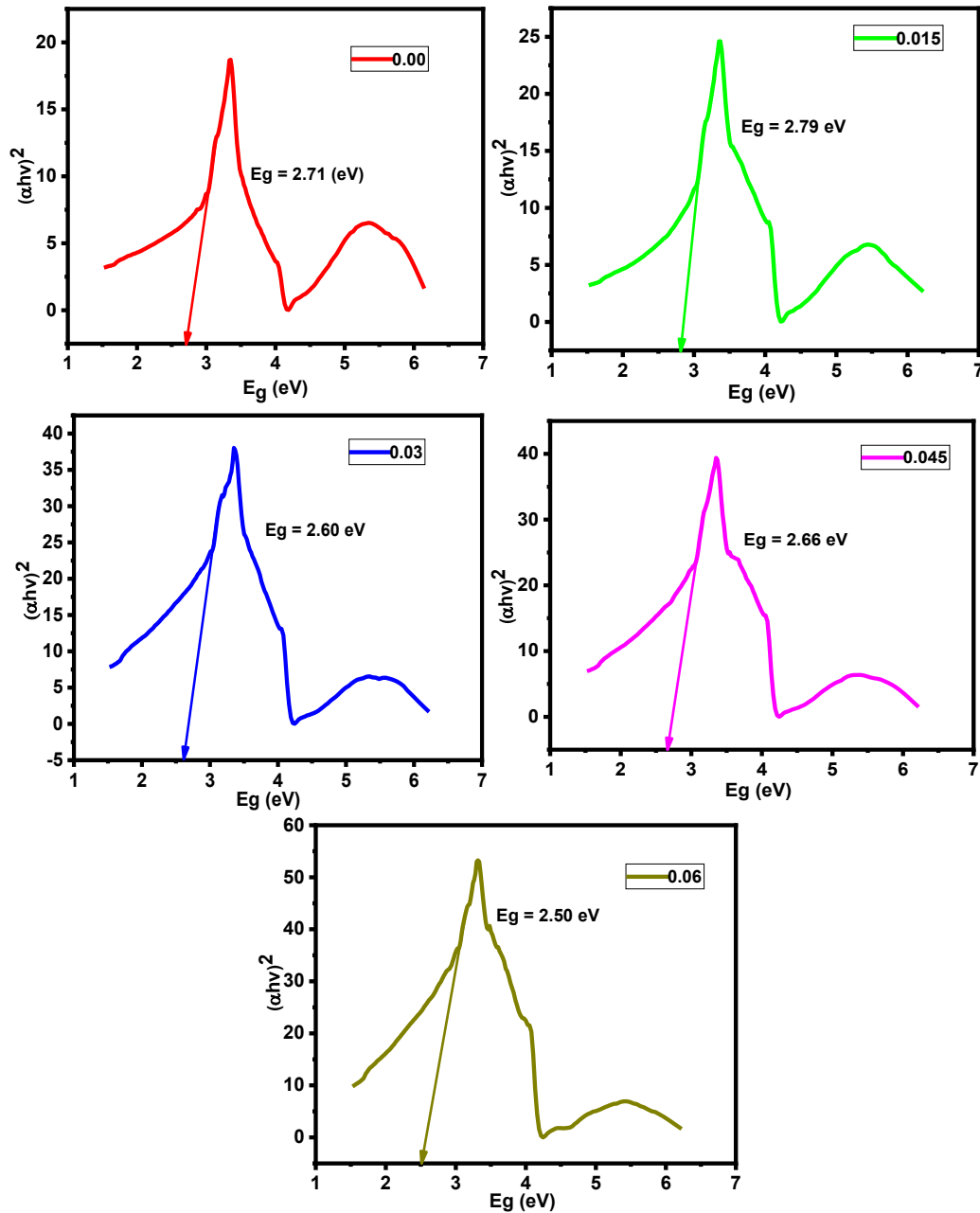

Fig. 5. Tauc plot for $Bi_{1-x}Dy_xFeO_3$ (x = 0.0, 0.015, 0.03, 0.045 and 0.06)

3.6. Raman analysis

The Raman spectra of Dy^{3+} substituted BFO ferrite acquired at room temperature are shown in Fig. 6. It was measured in order to understand more about its vibrational properties. Ferrites having a perovskite structure are included in the R3c group, which has eight formula units per unit cell. According to space group theory, the following group of optical phonon modes exist in ferrites at the Brillouin zone's center.i.e., $\Gamma = A_1g(R) + Eg (R) + T_1g + 3T_2g(R) + 2A_2u + 2Eu + 5T_1u(IR) + 2T_2u$ [4]. The existence of an inversion center in the centro-symmetrical space group R3c for the same vibrational mode demonstrates the mutual exclusion of Raman (R) and Infrared (IR) activity. Eg, (R), and 3T2g are the first five active modes seen in the Raman spectra (R). In addition to symmetry to the center of inversion, the notations A, E, T, and g stand for one-, two-,

and three-dimensional representations, respectively. In Dy^{3+} substituted BFO ferrite samples, five active modes are seen along with a number of additional vibrational modes that do not correspond to any of the active five modes (Fig. 6). (28).
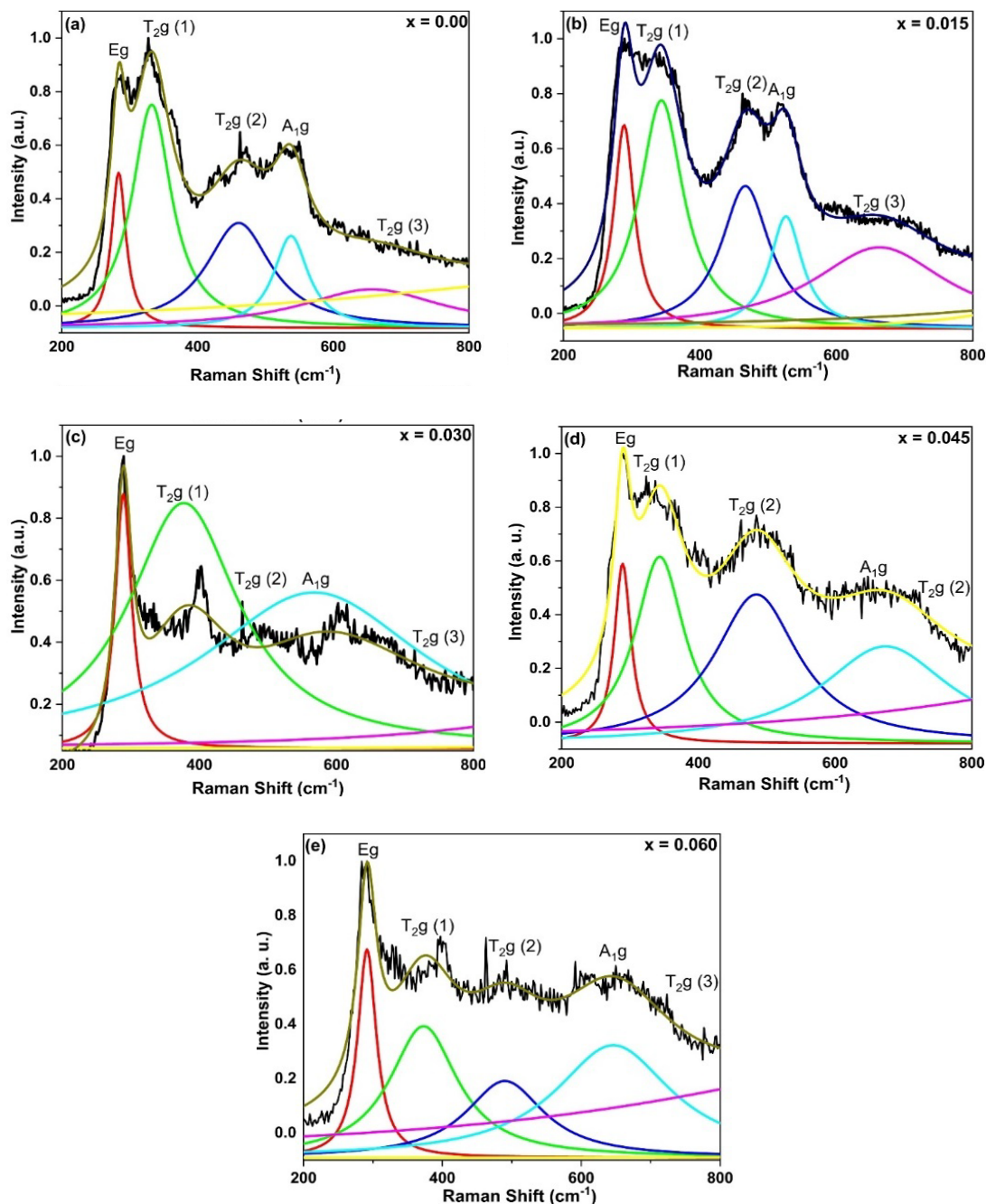

Fig. 6. (a-e). Raman spectra of room-temperature samples of bismuth ferrite.

The existence of such modes in lattice defects or crystal structure is related to dislocations, impurities, and lattice deformation. Although the XRD spectra reveal a single-phase structure, the presence of such bands is thought to be further evidence of crystal field deformation. The Raman modes, which depend on a loss of symmetry, are produced by a change in polarizability during molecule vibration in the crystal field [29]. T_2g (3) emerges at 678.83 - 682.18 cm^{-1} and is caused by symmetric and asymmetric bending of O_2 to Fe. While g is the symmetric bending of O_2 to Fe and is seen at 285.77-287.15 cm^{-1}, T_2g (2) appears at 461.83-469.71 cm^{-1} and is caused by an

antisymmetric stretching of Fe [30]. A1g emerges at 534.98-539 and is caused by the symmetric stretch of FeO_3. The broadening of the peaks is due to the asymmetric response of the crystal field as measured by vibrating dipoles. As a result, we assume that it broadens the idea of the deformed crystal structure [30].

3.7 Dielectric properties
3.7.1 Dielectric constant (Ɛ') and tangent loss (tanδ)

The room temperature $Bi_{1-x}Dy_xFeO_3$ was invested to evaluate the dielectric behavior based on frequency. $\varepsilon' = \frac{Cs}{Co}$ $Where$ $Co = \frac{A\varepsilon_\circ}{d}$

At higher frequencies, the dielectric constant behavior of all samples stays virtually constant. Grain, space charge polarization, and the conversion of Fe^{+2} to Fe^{+3} ferric ions all have an impact on the dielectric constant's linear behavior. As a result, the samples all had a high dielectric constant at the lower frequency. The grain boundary, dislocation, polarization of the space charge, and the high energy required to hope the electrons all have an impact on the dielectric constant's dispersion. There are certain resonance peaks in the lower frequency range, where the dielectric constant is smaller than in the high frequency range. As the concentration of Fe^{2+} ions at various lattice locations grows, so does the rate of electron transfer from Fe^{2+} to Fe^{3+}. The natural frequency and the applied frequency of the field become the same when ions oscillate evenly on both sides, power loss rises, and resonance peaks arise. Both Koop's theory and the well-known Maxwell-Wagner equations lend credence to this idea. Ferrites exhibit phases with increased conductivity due to the grains and phases with reduced conductivity due to the grain boundaries [31-32].
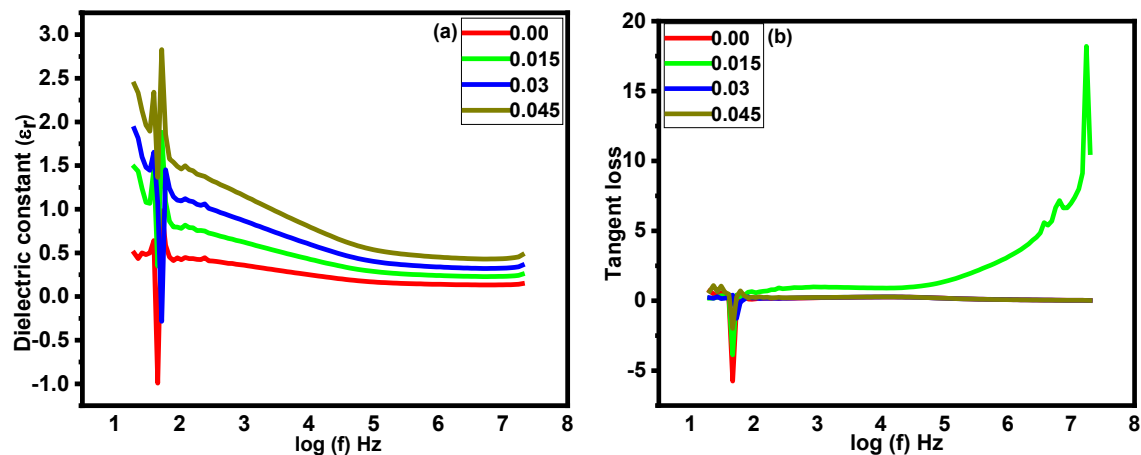

Fig. 7. Depicts the behavior of tangent loss as a function of frequency from 20 Hz to 20 MHz (b).

Tanδ is a concept used to describe how electrical energy is lost at different frequencies in dielectric materials.

$$\tan\delta = \frac{1}{\omega Cs Rs} \tag{9}$$

Each sample of Sr-doped bismuth ferrite's tangent was determined using Equation (2) and the formula.

The biggest tangent loss was seen in all samples at a very low frequency, and it became less as the frequency went up. Tan diminishes more quickly at lower frequencies than at higher ones. There is a significant loss because moving electrons from Fe^{2+} to Fe^{3+} needs more energy [33]. Dielectric loss may be caused by a variety of parameters, including Fe^{2+} concentration, composition, stoichiometry, and annealing temperature, among others. The same as in past experiments, tan lowers by introducing a high level of Dy^{3+} doping material at a very low frequency of 20 kHz [34-35]. These resonance peaks are assumed to be the consequence of

electron hopping at the octahedral sites between ferric and ferrous ions, which is the conduction mechanism [36-38].

3.7.2. AC conductivity and Impedance

The greatest way to assess a material's electrical characteristics as they change with composition, temperature, and frequency is via conductivity. The following formula considers ac conductivity.

$$\sigma_{ac} = \omega \varepsilon_{\circ} \, \varepsilon' \, \tan\delta \tag{10}$$

where the vacuum permittivity is o and the angular frequency is [4]. Figure 8(a) depicts the behavior of ac conductivity as a function of frequency from 20 Hz to 20 MHz for samples of bismuth ferrite doped with Dy^{3+}. At low frequencies, a smooth, frequency-independent zone was seen, whereas at higher frequencies, dispersion was observed. Ions hop at a low frequency from one location to the nearest location because they are available for a long time [38]. Fig. 6 depicts the increase in ac conductivity at various levels of dysprosium (Dy^{3+}) (a). The increase in ac conductivity was caused by the ionic radii of Dy^{3+} (0.91Å) and Bi^{3+} (1.17 Å). Due to an increase in charge carriers, maximum ac conductivity values were found at B-site. This occurred as a result of the dense microstructure. Low conductivity is caused by conduction, which is cation hopping among Fe^{3+} and Fe^{2+}. Due to the grain boundary and greater cation hopping, as seen in Fig. 6, the ac conductivity increased with increasing frequency [39] [40] [41]. Because it helps to separate grains from grain boundaries, complex impedance study is often used in polycrystalline materials. Figure 8 illustrates how impedance (Z) changes with frequency and doping levels (b). The highest impedance was seen at low frequencies. The remarkable responsiveness of grain boundaries to low-frequency noises is confirmed by the high impedance. When frequency is raised, the Z exhibits declining behavior, which might be caused by conductivity. Actually, impedance is the circuit resistance that moves in the opposite direction of ac conductivity. The overwhelming sensitivity of grain boundaries to low-frequency signals was confirmed by the enhanced impedance in the low-frequency band[42].
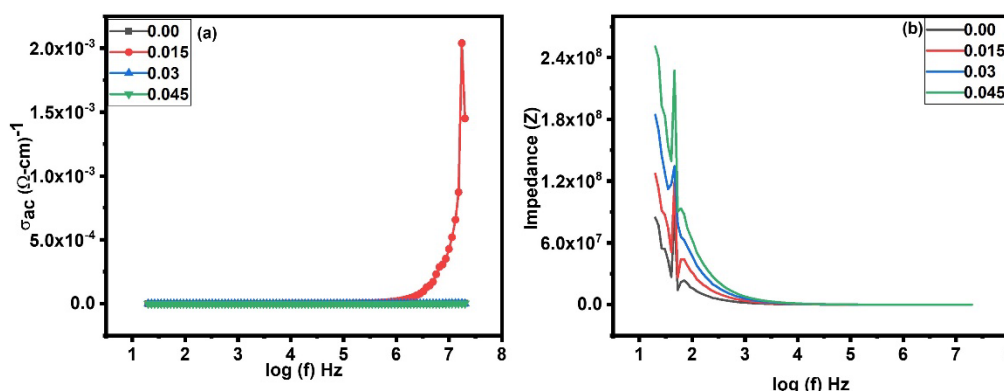

Fig. 8. Plot of (a) AC conductivity and (b) Impedance against frequency log (f).

Fig. 9 depicts the frequency-dependent fluctuation of the real component of the modulus M' (a). M has a low value at a lower frequency. For all samples, the value of M' rises with frequency, peaking at a constant maximum of M=1/ for higher frequencies. These results may be explained by the absence of restoring force, which is in charge of the movement of charges when an electric field is formed. These characteristics show that the material is not much affected by electrode polarization [43]. Due to the charge carriers' long-range mobilities, such behavior encourages conduction. At room temperature, Figure 9 shows the imaginary component of the electric modulus' frequency-dependent variation (b). A peak in the virtual component denoted by M″ provides details regarding conductivity relaxation, a charge transport process. The successful

charge carrier hopping took place below the low-frequency side of the peak. The potential was found to include charge carriers with short-ranged, constrained movements far above the peak frequency. Peaks that go up in frequency suggest a positive correlation between ion mobility and frequency [4]. Additionally, a peak in the modulus spectrum suggests conductivity relaxation [37].
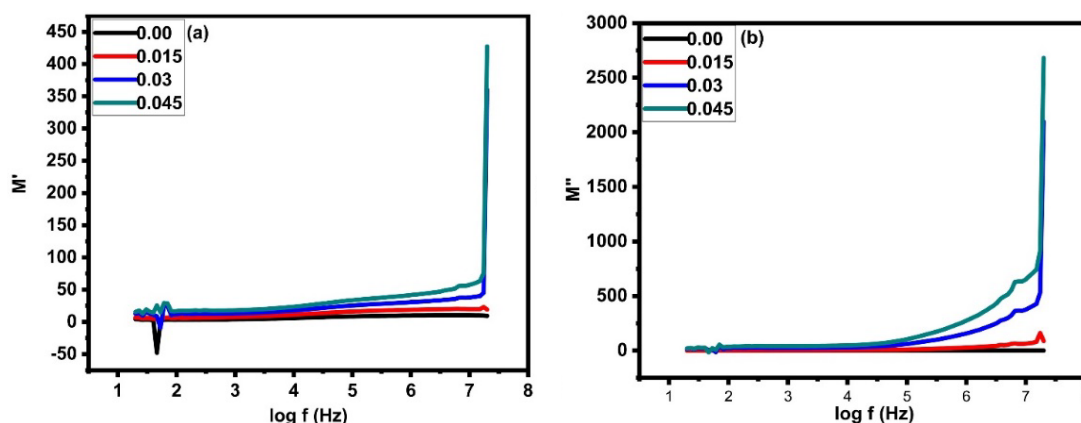

Fig. 9. Real (M) and Imaginary parts of Electric modulus for all samples of Dy doped Bismuth ferrites.

4. Conclusions

In this research project, the auto combustion method was successfully employed to produce Dy substituted $Bi_{1-x}Dy_xFeO_3$, and the ready samples were sintered at 600°C for three hours. The X-ray Diffraction Technique (XRD) and Raman spectra were used to study the microstructural characteristics. The XRD and Raman spectra of the created materials support the perovskite structure with Phase group R3c. The average crystallite size and the increase in crystallite size brought on by adding additional dysprosium to BFO were calculated using the Sherrer formula. The grain growth, which was almost in accordance with the XRD data, has been elucidated by the morphological results. At low frequency, the greatest dielectric constant was seen, and as frequency increases, it decreases. This material is particularly useful for technological applications because to doping variations in its dielectric characteristics.

References

[1] N.A. Hill, Why are there so few magnetic ferroelectrics?, J. Phys. Chem. B. 104(19) (2000) 6694-6709; https://doi.org/10.1021/jp000114x

[2] N.A. Spaldin, S. Cheong, R. Ramesh, Multiferroics : Past , present , and future feature, 63(10), 38-43 (2010); https://doi.org/10.1063/1.3502547

[3] E. Veena, A. Mallikarjuna, D.B. Basha, M.C. Sekhar, T. Rajender, G. Sujatha, T.A. Babu, N.V.K. Prasad, B.V.S. Reddy, S. Arabia, Structure , morphology , and ferroelectric behavior of Ba 1-y Zn y TiO 3, 17(1), 317–322 (2022).

[4] S. Pattanayak, B.N. Parida, P.R. Das, R.N.P. Choudhary, Impedance spectroscopy of Gd-doped BiFeO3 multiferroics, Appl. Phys. A Mater. Sci. Process. 112(2) 387-395 (2013); https://doi.org/10.1007/s00339-012-7412-6

[5] M.M. Rashad, Effect of synthesis conditions on the preparation of BiFeO 3 nanopowders using two different methods, 23(4), 882-888 (2012); https://doi.org/10.1007/s10854-011-0513-8

[6] T.S. Tlemc, Effect of Nd substitution on physical properties of multiferroic compound BiFeO 3,73(3), 673-678 (2015); https://doi.org/10.1007/s10971-015-3654-z

[7] M.Y. Shami, M.S. Awan, M. Anis-ur-rehman, Phase pure synthesis of BiFeO 3 nanopowders using diverse precursor via co-precipitation method, J. Alloys Compd. 509(41) 10139-10144 (2011); https://doi.org/10.1016/j.jallcom.2011.08.063

[8] J. Wei, D. Xue, Low-temperature synthesis of BiFeO 3 nanoparticles by ethylenediaminetetraacetic acid complexing sol - gel process, 43(12) 3368-3373 (2008); https://doi.org/10.1016/j.materresbull.2008.02.009

[9] C. Chen, J.C. Ã, S. Yu, L. Che, Z. Meng, Hydrothermal synthesis of perovskite bismuth ferrite crystallites, 291(1), 135-139 (2006); https://doi.org/10.1016/j.jcrysgro.2006.02.048

[10] T. Hussain, S.A. Siddiqi, S. Atiq, M.S. Awan, Induced modifications in the properties of Sr doped BiFeO3 multiferroics, Prog. Nat. Sci. Mater. Int. 23(5) 487-492 (2013); https://doi.org/10.1016/j.pnsc.2013.09.004

[11] S. Godara, N. Sinha, G. Ray, B. Kumar, Combined structural, electrical, magnetic and optical characterization of bismuth ferrite nanoparticles synthesized by auto-combustion route, J. Asian Ceram. Soc. 2(4) 416-421 (2014); https://doi.org/10.1016/j.jascer.2014.09.001

[12] M. Amin, H.M. Rafique, M. Yousaf, S.M. Ramay, M. Saleem, S.K. Abbas, S. Atiq, Multiferroicity in sol-gel synthesized Sr/Mn co-doped BiFeO3 nanoparticles, J. Mater. Sci. Mater. Electron. 28(22), 17234-17244(2017); https://doi.org/10.1007/s10854-017-7654-3

[13] Z. Li, Z. Hou, W. Song, X. Liu, D. Wang, J. Tang, Mg-substitution for promoting magnetic and ferroelectric properties of BiFeO 3 multiferroic nanoparticles, Mater. Lett. 175(14) 207-211 (2016); https://doi.org/10.1016/j.matlet.2016.04.016

[14] M. V. Shisode, J.S. Kounsalye, A. V. Humbe, R.C. Kambale, K.M. Jadhav, Investigations of magnetic and ferroelectric properties of multiferroic Sr-doped bismuth ferrite, Appl. Phys. A Mater. Sci. Process. 124, 0 (2018); https://doi.org/10.1007/s00339-018-2025-3

[15] M. Ishaque, M. Azhar, I. Ali, M. Athair, H.M. Khan, M.A. Iqbal, M.U. Islam, M. Farooq, Materials Science in Semiconductor Processing Synthesis of nickel - zinc - yttrium ferrites : Structural elucidation and dielectric behavior evaluation, Mater. Sci. Semicond. Process. 41(7) 508-512 (2016); https://doi.org/10.1016/j.mssp.2015.10.028

[16] C. Ferrite, N. Prepared, C. Method, Effect of Temperature on Structural , Magnetic and Dielectric Properties of Effect of Temperature on Structural , Magnetic and Dielectric Properties of Cobalt Ferrite Nanoparticles Prepared via Co-precipitation Method, (2015).

[17] G. Mustafa, M. Khalid, A. Dad, C. Kiran, S. Zaheer, Dielectric , impedance , and modulus spectroscopic studies of lanthanum-doped nickel spinel ferrites NiLa x Fe 2- x O 4 nanoparticles,12(2) 596-605 (2022); https://doi.org/10.1007/s10971-020-05359-z

[18] G. Hussain, I. Ahmed, A.U. Rehman, M.U. Subhani, N. Morley, M. Akhtar, M.I. Arshad, H. Anwar, Study of the role of dysprosium substitution in tuning structural, optical, electrical, dielectric, ferroelectric, and magnetic properties of bismuth ferrite multiferroic, J. Alloys Compd. 165743 (2022); https://doi.org/10.1016/j.jallcom.2022.165743

[19] I. Ahmed, G. Mustafa, M. Umair Subhani, G. Hussain, A.G. Ismail, H. Anwar, A detailed investigation of lanthanum substituted bismuth ferrite for enhanced structural, optical, dielectric, magnetic and ferroelectric properties, Results Phys. 38(1), 105584 (2022); https://doi.org/10.1016/j.rinp.2022.105584

[20] A.B. Mugutkar, S.K. Gore, U.B. Tumberphale, V. V. Jadhav, R.S. Mane, S.M. Patange, S.F. Shaikh, M. Ubaidullah, A.M. Al-Enizi, S.S. Jadhav, The role of La3+ substitution in modification of the magnetic and dielectric properties of the nanocrystalline Co-Zn ferrites, J. Magn. Magn. Mater. 502, 166490 (2020); https://doi.org/10.1016/j.jmmm.2020.166490

[21] B.B.R. Shaikh, B.G. Toksha, S.E. Shirsath, A. Chatterjee, S. Tonde, S.Q. Chishty, Microstructure, magnetic, and dielectric interplay in NiCuZn ferrite with rare earth doping for magneto-dielectric applications, J. Magn. Magn. Mater. 537, 168229 (2021); https://doi.org/10.1016/j.jmmm.2021.168229

[22] J. Balavijayalakshmi, N. Suriyanarayanan, R. Jayapraksah, In fl uence of copper on the

magnetic properties of cobalt ferrite nano particles, Mater. Lett. 81(21), 52-54 (2012); https://doi.org/10.1016/j.matlet.2012.04.076

[23] M.A. Malana, R.B. Qureshi, M.N. Ashiq, Synthesis , electrical and dielectric characterization of cerium doped nano copper ferrites, Mater. Res. Bull. 48(3) 4775-4779 (2013); https://doi.org/10.1016/j.materresbull.2013.08.021

[24] G. Mustafa, M.U. Islam, W. Zhang, Y. Jamil, A.W. Anwar, M. Hussain, M. Ahmad, Investigation of structural and magnetic properties of Ce3+-substituted nanosized Co-Cr ferrites for a variety of applications, J. Alloys Compd. 618(15) 428-436 (2015); https://doi.org/10.1016/j.jallcom.2014.07.132

[25] S.I. Ahmad, S.A. Ansari, D. Ravi Kumar, Structural, morphological, magnetic properties and cation distribution of Ce and Sm co-substituted nano crystalline cobalt ferrite, Mater. Chem. Phys. 208(12), 248-257 (2018); https://doi.org/10.1016/j.matchemphys.2018.01.050

[26] S. Kumar, G. Srivastava, G. Almutairi, F. Ahmed, N.M. Shaalan, S. Dalela, R. Kumar, A.P. Kumar, P.A. Alvi, K.H. Chae, H.H. Hammud, K. Kumari, Electronic structure and electrochemical properties of La-doped BiFeO3 nanoparticles, J. Electron Spectros. Relat. Phenomena. 253(12) 147138 (2021); https://doi.org/10.1016/j.elspec.2021.147138

[27] M. Nadeem, W. Khan, S. Khan, S. Husain, F. Singh, A. Ansari, D.K. Shukla, A. Ahad, V.K. Chakradhary, M.J. Akhtar, Structural, optical and enhanced multiferroic properties of La/Cr co-substituted BiFeO3 nanostructures, J. Mater. Sci. Mater. Electron. 31(3) 11177-11194 (2020); https://doi.org/10.1007/s10854-020-03666-3

[28] A. Kumar, P. Sharma, D. Varshney, Structural, vibrational and dielectric study of Ni doped spinel Co ferrites: Co1-xNixFe2O4 (x=0.0, 0.5, 1.0), Ceram. Int. 40(4) 12855-12860 (2014); https://doi.org/10.1016/j.ceramint.2014.04.140

[29] M.H. Abdellatif, G.N. Abdelrasoul, M. Salerno, I. Liakos, A. Scarpellini, S. Marras, A. Diaspro, Fractal analysis of inter-particle interaction forces in gold nanoparticle aggregates, Colloids Surfaces A Physicochem. Eng. Asp. 497(52) 225-232 (2016); https://doi.org/10.1016/j.colsurfa.2016.03.013

[30] O.N. Shebanova, P. Lazor, Raman spectroscopic study of magnetite (FeFe2O4): A new assignment for the vibrational spectrum, J. Solid State Chem. 174(7) 424-430(2003); https://doi.org/10.1016/S0022-4596(03)00294-9

[31] S. Maensiri, Author ' s Accepted Manuscript Electrical and nonlinear current - voltage characteristics of La - doped BiFeO 3 ceramics, Ceram. Int. (2017).

[32] A. Saini, P. Kumar, B. Ravelo, S. Lallechere, A. Thakur, P. Thakur, Magneto-dielectric properties of doped ferrite based nanosized ceramics over very high frequency range, 23(3), 8-13 (2016).

[33] A. Khalid, M. Ali, G.M. Mustafa, S. Atiq, Structural and dielectric properties of sol - gel synthesized (Mn , Cu) co-doped BiFeO 3 ceramics, J. Sol-Gel Sci. Technol. (2016); https://doi.org/10.1007/s10971-016-4142-9

[34] S. Picozzi, C. Ederer, First principles studies of multiferroic materials, (2009); https://doi.org/10.1088/0953-8984/21/30/303201

[35] S. Chandel, P. Thakur, M. Tomar, V. Gupta, A. Thakur, Investigation of structural, optical, dielectric and magnetic studies of Mn substituted BiFeO3 multiferroics, Ceram. Int. 43(7) 13750-13758 (2017); https://doi.org/10.1016/j.ceramint.2017.07.088

[36] A.M.A. El Ata, M.K. El Nimr, D. El Kony, Dielectric and magnetic permeability behavior of BaCo Ni Fe O W-type hexaferrites \ V V, 20(4), 36-44 (1999); https://doi.org/10.1016/S0304-8853(99)00381-9

[37] C. Matter, Morphological , Raman , electrical and dielectric properties of rare earth doped X-type hexagonal ferrites Author ' s Accepted Manuscript, (2016).

[38] K. Kaswan, A. Agarwal, Author ' s Accepted Manuscript, Ceram. Int. 0-25 (2015).

[39] A.K. Behera, N.K. Mohanty, S.K. Satpathy, B. Behera, P. Nayak, Effect of Rare Earth Doping on Impedance , Modulus and Conductivity Properties of Multiferroic Composites :, Acta

Metall. Sin. (English Lett. 5 (2015).

[40] K. Hussain, N. Amin, M.I. Arshad, Evaluation of structural , optical , dielectric , electrical , and magnetic properties of Ce 3 + doped Cu 0 . 5 Cd 0 . 25 Co 0 . 25 Fe 2-x O 4 spinel nano-ferrites, Ceram. Int. (2020);
https://doi.org/10.1016/j.ceramint.2020.09.185

[41] S. Jangra, S. Sanghi, A. Agarwal, M. Rangi, K. Kaswan, E ff ects of Nd 3 + and high-valence Nb 5 + co-doping on the structural , dielectric and magnetic properties of BiFeO 3 multiferroics, (2018); https://doi.org/10.1016/j.ceramint.2018.01.194

[42] M. Amin, H.M. Rafique, M. Yousaf, S.M. Ramay, S. Atiq, Structural and impedance spectroscopic analysis of Sr/Mn modified BiFeO3 multiferroics, J. Mater. Sci. Mater. Electron. 27(3) 11003-11011 (2016);
https://doi.org/10.1007/s10854-016-5216-8

[43] S.S. Ionics, R. Workshop, S. State, I. Batteries, ac Conductivity Analysis of Glassy Silver Iodomolybdate System ~r B.V.R Chowdari and R. Gopalakrishnan Department of Physics, National University of Singapore, Singapore 0511, 23(4) 225-233 (1987);
https://doi.org/10.1016/0167-2738(87)90055-5

[44] A. Ianculescu, F. Prihor, P. Postolache, The role of doping on the structural and functional properties of BiFe 1 − x Mn x O 3 magnetoelectric ceramics, 504(2), 420-426 (2010);
https://doi.org/10.1016/j.jallcom.2010.05.135